Chinese Journal of Aeronautics, (2015),28(1): 93–102

Chinese Society of Aeronautics and Astronautics
& Beihang University

Chinese Journal of Aeronautics

cja@buaa.edu.cn
www.sciencedirect.com

Numerical study on flow fields and aerodynamics of tilt rotor aircraft in conversion mode based on embedded grid and actuator model

Zhang Ying *, **Ye Liang, Yang Shuo**

Aviation Key Laboratory of Science and Technology on Aerodynamics of High Speed and High Reynolds Number, AVIC Aerodynamics Research Institute, Shenyang 110034, China

Received 22 January 2014; revised 20 June 2014; accepted 3 September 2014
Available online 26 December 2014

KEYWORDS

Actuator disk;
Conversion mode;
Embedded grid;
Grid assembling;
Tilt rotor aircraft

Abstract A method combining rotor actuator disk model and embedded grid technique is presented in this paper, aimed at predicting the flow fields and aerodynamic characteristics of tilt rotor aircraft in conversion mode more efficiently and effectively. In this method, rotor's influence is considered in terms of the momentum it impacts to the fluid around it; transformation matrixes among different coordinate systems are deduced to extend actuator method's utility to conversion mode flow fields' calculation. Meanwhile, an embedded grid system is designed, in which grids generated around fuselage and actuator disk are regarded as background grid and minor grid respectively, and a new method is presented for 'donor searching' and 'hole cutting' during grid assembling. Based on the above methods, flow fields of tilt rotor aircraft in conversion mode are simulated, with three-dimensional Navier–Stokes equations discretized by a second-order upwind finite-volume scheme and an implicit lower–upper symmetric Gauss–Seidel (LU-SGS) time-stepping scheme. Numerical results demonstrate that the proposed CFD method is very effective in simulating the conversion mode flow fields of tilt rotor aircraft.

1. Introduction

Tilt rotor aircraft is a flight vehicle which can land and take off vertically, as well as convert to propeller mode to achieve high-speed cruise performance. Extensive researches, covering a number of areas including aerodynamic interactions, performance, aeroacoustics and dynamics, have been conducted on it in recent years due to its unique advantages and technical complexity. In the aspect of experimental research, various experiments have been carried out by NASA Ames Research Center, Bell Helicopters Inc.[1–3] and other institutions. Abundant experimental data has been obtained, which provides great assistance to the tilt rotor aircraft design and manufacture. In the aspect of computational research, due to the complexities of tilt rotor flow fields and its aerodynamic characteristics, more and more researchers started to study tilt

* Corresponding author. Tel.: +86 24 86566610.
E-mail address: zyzq6583@126.com (Y. Zhang).

Peer review under responsibility of Editorial Committee of CJA.

Production and hosting by Elsevier

http://dx.doi.org/10.1016/j.cja.2014.12.028
1000-9361

rotor aircraft aerodynamics by solving Navier–Stokes equations instead of using conventional methods. For example, in the mid-1990s, the flow field of V-22 rotor/wing configuration in hover was simulated by Meakin[4] with the unsteady thin-layer Navier–Stokes equations, and rotor motion and rotor/airframe interference were simulated directly using moving body overset grid methods. The flow over a wing-fuselage-nacelle configuration of the V-22 tilt rotor aircraft in forward flight was simulated by Tai[5] with a multi-zone, thin-layer Navier–Stokes method, and major flow features including the three-dimensional flow separation due to viscous-vortex interactions observed experimentally were captured. After the year 2000, overset-grid Reynolds Averaged Navier–Stokes (RANS) solvers, OVERFLOW and Fun3D, were used by Gupta and Baeder[6] and Lee-Rausch[7] respectively to numerically simulate the flow fields of a simplified Quad Tilt Rotor (QTR) in forward flight and an isolated tilt rotor in hover. Aerodynamic characteristics of tilt rotor in hover were computed by Potsdam and Strawn[8] by solving the governing equations in rotation reference frame. More detailed investigations on tilt rotor aircraft were presented in the doctorate thesis of Gupta.[9] In his paper, flow fields around a simplified Quad Tilt rotor, both in and out of ground effect, were simulated; rotor was modeled by both actuator disk and body conforming meshes method, the results obtained by these two methods were then compared.

A feature of tilt rotor aircraft is the existence of conversion mode. In this status, the manipulation and dynamic response of its blades are more complex than those of conventional helicopter rotors or propeller because of the more severe wake distortion and unsteady blade loads. Research on tilt rotor aircraft in conversion mode is still a challenge until now, although extensive research works on this aircraft in helicopter or propeller mode have been conducted. Challenges to the research work on tilt rotor aircraft arise from the complexity of flow physics in conversion mode, which is reflected in the following two aspects. One is that the rotor wake is intensely distorted due to the blade manipulation for aerodynamic balance and the other is that flow fields induced by wing and rotors are closely coupled and severe aerodynamic interference phenomenon appears, with the reason that the forward flight speed is usually not very high and the space between rotor blades and wings is quite narrow.

Considering the importance and complexity of the research on conversion mode, this paper mainly focuses on numerical methods to be used for conversion mode simulation. In general, accurate modeling of flow around individual rotor blades is a complex task even for a conventional helicopter configuration, which means much more time and resource requirements for tilt rotor aircraft conversion mode calculation. As the first step of the research plan, this paper proposes a new approach by combining rotor actuator disk model with embedded grid technique, aimed at providing a rapid, effective and universal method, which can be conveniently transplanted to the rotor blade body-fitted flow field calculation in future. The work in this paper can be described as follows: rotor is modeled as an actuator disk in order to ameliorate computational time costs and make simulation works possible, and transformation matrixes among different coordinate systems are deduced so that the actuator model can be used at different tilt angles. Meanwhile, embedded grid system is designed to describe relative movement among the rotors and wing/fuselage, and a new method is presented for 'donor searching' and 'hole cutting' during grid assembling. Grids generated around fuselage and actuator disk are regarded as background grid and minor grid respectively, and the influence of actuator disk on flow fields at different tilt angles is simulated by the location change of minor gird.

A CFD solver is put forward after comprehensively analyzing the requirements of flow field calculation for tilt rotor configurations in conversion mode, by combining methods mentioned above and Navier–Stokes equations solving technique. Three-dimensional Navier–Stokes equations are discretized using a second-order upwind finite-volume scheme and an implicit LU-SGS scheme. Induced velocity fields of experimental rotors are simulated firstly for validation purpose, and then flow fields of a tilt rotor aircraft model are calculated. Results indicate that the present CFD method is very effective and has the ability to capture essential flow field characteristics and to predict aerodynamic interactions of tilt rotor aircraft in conversion mode.

2. Methodology

2.1. Grid system

An embedded grid system with the rotor modeled as actuator disk is adopted in the present work. Considering the relative movement among different components of tilt rotor configurations, a minor grid with the rotor modeled as actuator disk and a background grid enclosing unmoving bodies (fuselage) are generated separately, and the minor grid is fully embedded inside the background grid. Taking the universality into consideration, topology of grid cells is not restricted (although the pure hexahedron cells are used in the following illustrations).

Preprocessing of overset grid conventionally involves two steps: 'hole cutting' and 'donor searching'. The related previous investigations are extensive and various methods are developed, such as explicit and implicit methods for hole cutting,[10–12] inverse map,[13] neighbor-to-neighbor (N2N)[14] and alternating digital tree (ADT) searching algorithm[15] for donor cell searching. Based on these previous studies, a more adaptable scheme is designed and applied in the present work to meet the requirements for tilt rotor aircraft calculation as described in detail as follows.

(1) For each grid block, cells which are directly adjacent to body surface or actuator disk are marked as layer 1; those unmarked cells which are adjacent to layer 1 are then marked as layer 2. Then, the left cells will be marked with different layer numbers according to the method, and these layer numbers will be used as adaptable parameters for adjusting range of 'hole cutting'.
(2) For each cell (noted as C) in one grid block, cell in other grid blocks which contains the cell center of C is searched and noted as donor cell (D). If the layer number of cell D is less than or equal to a given constant, cell C will be regarded as 'Hole Cell', which should be blanked out during computation. Those cells which do not have donor cells are temporarily considered as normal cells. Neighbor-to-Neighbor (N2N) searching algorithm is adopted for donor cell searching and the

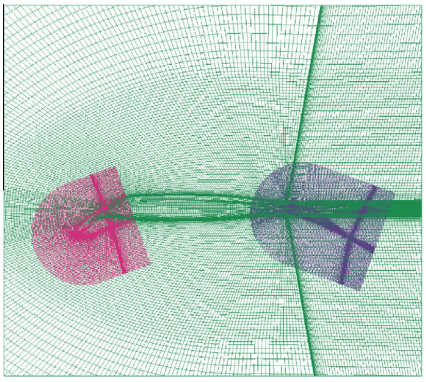

Fig. 1 Grids before hole cutting.

efficiency of this algorithm relies on the start location of donor cell. For problems concerning grid motion, recalculation of the domain connectivity, including hole cutting and interpolation coefficients at each time step is required, and information from the previous time step is reused instead of domain connectivity solutions from scratch to enable speed-ups. Furthermore, as we know neighbor-to-neighbor algorithm performs well only when the domain is continuous and convex, so in order to satisfy this condition, auxiliary gird is generated inside body and the convexity of outer boundary of each grid block must be ensured.

(3) For loop over all normal cells, the cell whose neighbors have 'Hole Cell' is defined as 'Interpolated Cell'.

A multi-element airfoil model (as shown in Fig. 1) is used to better elucidate this embedded grid technique. Gird enclosing the main wing is defined as background grid, while grids around leading-edge slat and flap are defined as minor grids. It can be seen from this figure that some minor grids cells (some of them are outer boundary cells) overlapping in-body region of background grid must be blanked out. Remaining outer boundary of the minor grid blocks gets information from background grid, which acts as a boundary condition for the minor grid. Meanwhile, holes are cut in the background grid in those regions where the finer near body grid (minor grid) is available; since hole is cut at the background grid, an inner boundary is generated in the background grid and those cells need to receive information from the minor grid. A typical searching path adopted to find donor cell for an arbitrary cell is shown in Fig. 2 and the arrows demonstrate the searching direction. Fig. 3 is the grids after 'hole cutting' and Fig. 4 shows background grid after hole cutting by using different layer numbers.

2.2. Numerical method

2.2.1. Governing equations

For a three-dimensional flow through a finite volume Ω moving with a speed V_t, which is enclosed by the boundary surface $\partial\Omega$ and an exterior normal vector $\boldsymbol{n}$, integral form of the conservation equations in inertial reference frame is given as

$$\frac{\partial}{\partial t}\int\int\int \boldsymbol{W}\mathrm{d}\Omega + \oiint_{\partial\Omega}(\boldsymbol{F}-\boldsymbol{W}V_t)\cdot\boldsymbol{n}\mathrm{d}S = \boldsymbol{Q} \tag{1}$$

where $\boldsymbol{W}$ denotes the vector of conservative variables, $\boldsymbol{F}$ convective flux vector, and $\boldsymbol{Q}$ source term. These vectors are given below:

$$\begin{cases} \boldsymbol{W} = [\rho, \rho\boldsymbol{V}, \rho E]^{\mathrm{T}} \\ \boldsymbol{F} = [\rho\boldsymbol{V}\cdot\boldsymbol{n}, \rho\boldsymbol{V}(\boldsymbol{V}\cdot\boldsymbol{n})\cdot\boldsymbol{n} + P\boldsymbol{n}, \\ \quad \rho E(\boldsymbol{V}\cdot\boldsymbol{n}) + P\boldsymbol{V}\cdot\boldsymbol{n}]^{\mathrm{T}} \end{cases}$$

where ρ denotes the density, $\boldsymbol{V}$ vector of velocity, E total energy per unit mass and P pressure.

2.2.2. Definition and transformation of coordinate systems

Three different coordinate systems are adopted for describing the movement of a tilt rotor aircraft: inertial reference frame, nacelle reference frame and rotor reference frame (see Fig. 5). The inertial reference frame convention used in the present work is given in detail as follows: z-axis: longitudinal fuselage which is positive in downstream direction; y-axis: vertical direction of fuselage which is positive upward; x-axis: spanwise axis (parallel to the tilt axis of nacelle).

Transformation matrixes between different coordinate systems are given as follows:

$$\boldsymbol{M}_1 = \begin{bmatrix} 1 & 0 & 0 \\ 0 & \cos\gamma & \sin\gamma \\ 0 & -\sin\gamma & \cos\gamma \end{bmatrix} \boldsymbol{M}_2 = \begin{bmatrix} \cos\psi & 0 & -\sin\psi \\ 0 & 1 & 0 \\ \sin\psi & 0 & \cos\psi \end{bmatrix} \boldsymbol{M}_3 = \begin{bmatrix} 1 & 0 & 0 \\ 0 & \cos\beta & \sin\beta \\ 0 & -\sin\beta & \cos\beta \end{bmatrix} \boldsymbol{M}_4 = \begin{bmatrix} \cos\theta & \sin\theta & 0 \\ -\sin\theta & \cos\theta & 0 \\ 0 & 0 & 1 \end{bmatrix} \tag{2}$$

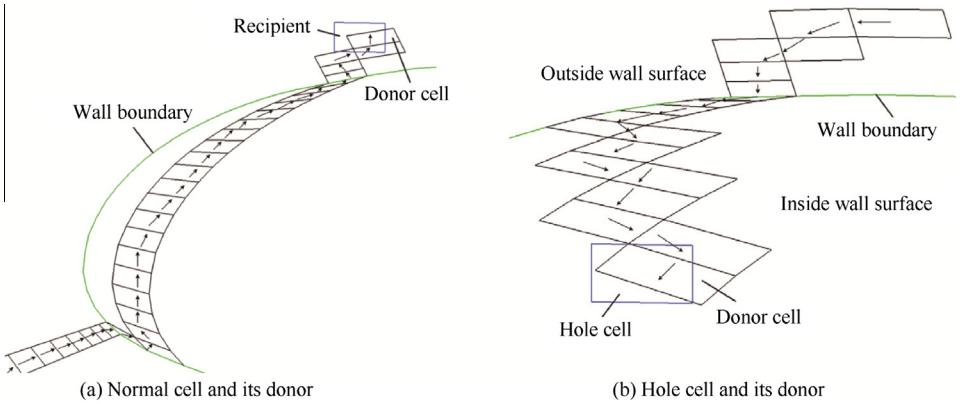

(a) Normal cell and its donor (b) Hole cell and its donor

Fig. 2 Searching path adopted to find the donor cell for an arbitrary cell.

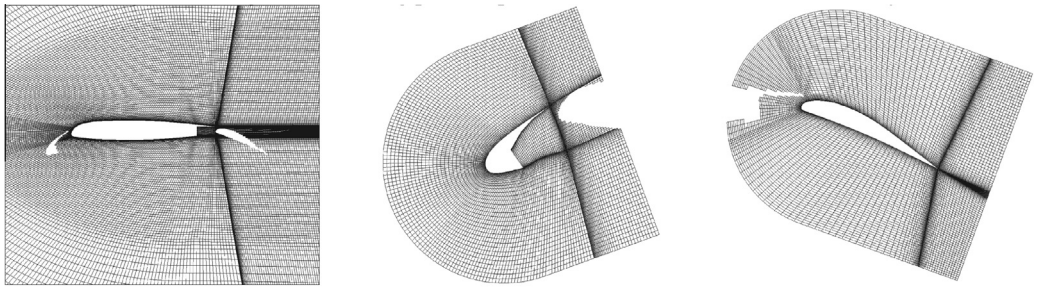

(a) Background grid (b) Leading-edge slat grid (c) Flap grid

Fig. 3 Grids after hole cutting.

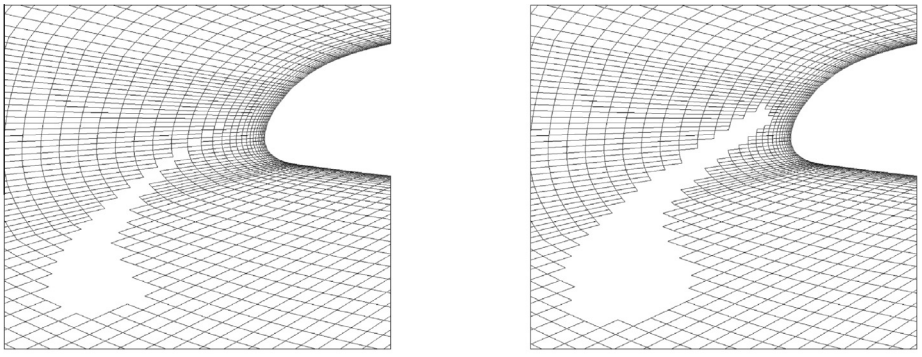

(a) Layer number=1 (b) Layer number=6

Fig. 4 Background grid after hole cutting with different layer numbers' selection.

where γ, ψ, β and θ are tilt angle, azimuthal angle, flap angle and pitch angle respectively.

Coordinate transformation between inertial reference frame and rotor reference frame can be written as

$$\begin{cases} \begin{bmatrix} x-x_{\mathrm{nrc}} \\ y-y_{\mathrm{nrc}} \\ z-z_{\mathrm{nrc}} \end{bmatrix} = [\boldsymbol{M}_1][\boldsymbol{M}_2][\boldsymbol{M}_3][\boldsymbol{M}_4] \begin{bmatrix} \xi-\xi_{\mathrm{rrc}} \\ \eta-\eta_{\mathrm{rrc}} \\ \zeta-\zeta_{\mathrm{rrc}} \end{bmatrix} \\ \qquad\qquad +[\boldsymbol{M}_1] \begin{bmatrix} \xi'_{\mathrm{rrc}}-\xi'_{\mathrm{nrc}} \\ \eta'_{\mathrm{rrc}}-\eta'_{\mathrm{nrc}} \\ \zeta'_{\mathrm{rrc}}-\zeta'_{\mathrm{nrc}} \end{bmatrix} \\ \begin{bmatrix} \xi-\xi_{\mathrm{rrc}} \\ \eta-\eta_{\mathrm{rrc}} \\ \zeta-\zeta_{\mathrm{rrc}} \end{bmatrix} = [\boldsymbol{M}_4]^{\mathrm{T}}[\boldsymbol{M}_3]^{\mathrm{T}}[\boldsymbol{M}_2]^{\mathrm{T}}[\boldsymbol{M}_1]^{\mathrm{T}} \begin{bmatrix} x-x_{\mathrm{nrc}} \\ y-y_{\mathrm{nrc}} \\ z-z_{\mathrm{nrc}} \end{bmatrix} \\ \qquad\qquad -[\boldsymbol{M}_4]^{\mathrm{T}}[\boldsymbol{M}_3]^{\mathrm{T}}[\boldsymbol{M}_2]^{\mathrm{T}} \begin{bmatrix} \xi'_{\mathrm{rrc}}-\xi'_{\mathrm{nrc}} \\ \eta'_{\mathrm{rrc}}-\eta'_{\mathrm{nrc}} \\ \zeta'_{\mathrm{rrc}}-\zeta'_{\mathrm{nrc}} \end{bmatrix} \end{cases} \tag{3}$$

where (x, y, z), (ξ, η, ζ) and (ξ', η', ζ') are coordinates in inertial reference frame, rotor rotating reference frame and nacelle rotating reference frame respectively; the subscript rrc and nrc denote rotor rotation center and nacelle rotation center.

2.2.3. Rotor modeling method

The rotor is modeled as an infinite thin disk[16] and there are two aspects which need to be considered in determining the rotor's influence on the flow field. One aspect is to find the locations in the physical or computational domain where the influence is felt. The other aspect is to determine the momentum equation source terms $\boldsymbol{Q}$ in Eq. (1) at these locations.

The actuator disk is treated as a separate plane in the flow field and discretized into small elements. For each element, there are two grid cells, locating above and below the element respectively. The force acting on an arbitrary element is denoted as (S_x, S_y, S_z) and distributed equally into the two grid cells. Consequently, the source term $(\boldsymbol{MS})_{\mathrm{K}}$ added

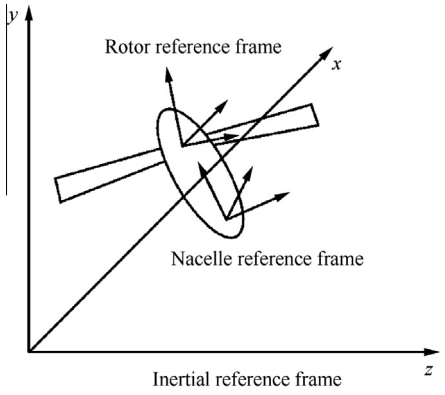

Fig. 5 Reference coordinate systems definition.

to the governing equations that is induced by the rotor's influence is written as

$$(\boldsymbol{MS})_{\mathrm{K}} = [0,\ \ S_x/2,\ \ S_y/2,\ \ S_z/2,\ \ (uS_x + vS_y + wS_z)/2]^T \tag{4}$$

where u, v, w denote velocity components.

Take a tiny element on the plane of actuator disk as the investigation object, which is located at a distance r from the center of hub, with a length of dr along the spanwise direction and a width of $\Delta\theta$ along the circumferential direction. Supposing that the force acting on the blade is d$\boldsymbol{F}$ the instantaneous force acting on the fluid element at this location is then $-$d$\boldsymbol{F}$ and the resultant force is $-N$d$\boldsymbol{F}$ for N blades. Consequently, the time averaged force acting on the surface of grid cell, whose area is S_Δ, is $[NS_\Delta(-\mathrm{d}\boldsymbol{F})/2\pi r]dr$. The rotational speed of rotor is $\boldsymbol{\omega}$ and flow velocity experienced by the airfoil in rotor reference frame is shown in Fig. 6 (Rotor rotation direction is clockwise or counter-clockwise when viewed from

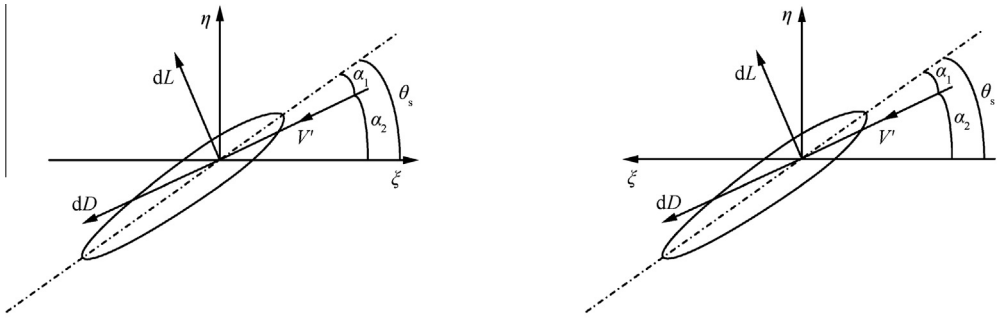

(a) Clockwise rotation (b) Counter-clockwise rotation

Fig. 6 Flow velocity experienced by the airfoil.

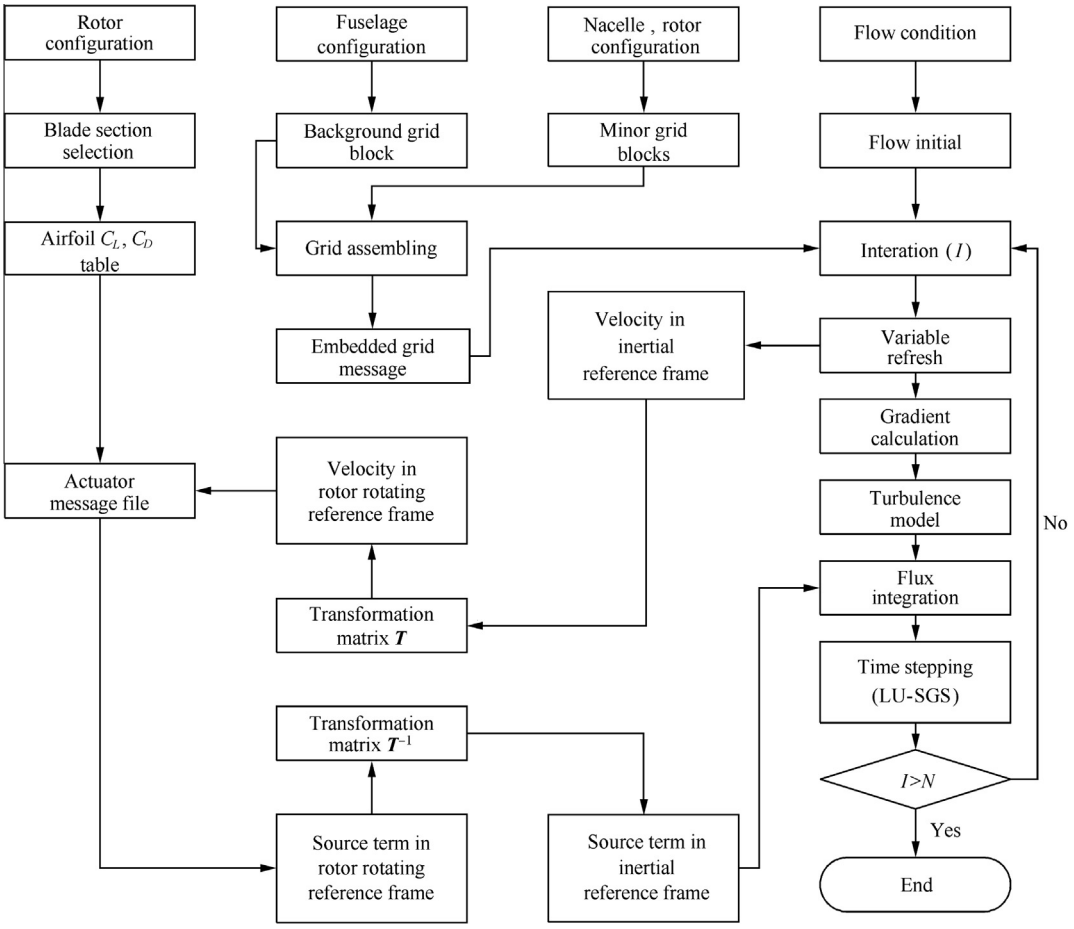

Fig. 7 Schematic of tilt rotor flow field calculation.

above the model), where α_1 is the effective angle of attack and θ_s is the initial collective angle.

Since there are no aerodynamic forces along the span (ζ direction), only forces along ξ and η directions need to be calculated (see Fig. 6). For a clockwise rotating rotor, the forces $f_{\Delta\xi}$ and $f_{\Delta\eta}$ acting on the surface of grid cell, along ξ and η directions, are written in Eq. (5).

$$\begin{cases} f_{\Delta\eta} = \frac{N(-\mathrm{d}F_\eta)S_\Delta}{2\pi r\mathrm{d}r} = \frac{-N(\mathrm{d}L\cos\alpha_2+\mathrm{d}D\sin\alpha_2)S_\Delta}{2\pi r\mathrm{d}r} \\ \quad = \frac{-N\left(\frac{1}{2}\rho V'^2 C_L c\mathrm{d}r\cos\alpha_2+\frac{1}{2}\rho V'^2 C_D c\mathrm{d}r\sin\alpha_2\right)S_\Delta}{2\pi r\mathrm{d}r} \\ \quad = \frac{-N\rho V'^2 cS_\Delta(C_L\cos\alpha_2+C_D\sin\alpha_2)}{4\pi r} \\ f_{\Delta\xi} = \frac{N(-\mathrm{d}F_\xi)S_\Delta}{2\pi r\mathrm{d}r} = \frac{-N(-\mathrm{d}L\sin\alpha_2+\mathrm{d}D\cos\alpha_2)S_\Delta}{2\pi r\mathrm{d}r} \\ \quad = \frac{-N\left(-\frac{1}{2}\rho V'^2 C_L c\mathrm{d}r\sin\alpha_2+\frac{1}{2}\rho V'^2 C_D c\mathrm{d}r\cos\alpha_2\right)S_\Delta}{2\pi r\mathrm{d}r} \\ \quad = \frac{-N\rho V'^2 cS_\Delta(-C_L\sin\alpha_2+C_D\cos\alpha_2)}{4\pi r} \end{cases} \tag{5}$$

where ρ is the density changing along with the flow fields' iterating, r the radial location, c the blade chord-length, S_Δ the area of grid cell, and V' relative resultant velocity in rotor reference frame; $\mathrm{d}L$ and $\mathrm{d}D$ are lift and drag acting on the blade, and C_L and C_D are lift and drag coefficient. $\alpha_2 = \arctan(V_\eta/V_\xi)$, where V_ξ and V_η are the components of V' along ξ direction and η direction respectively. Similar equations can be deduced for counter-clockwise rotating rotor.

2.2.4. Method for flux computation

ROE's scheme[17] is used in spatial discretization and flux function on the interface can be written as

$$\boldsymbol{F}^{\mathrm{ROE}}_{i+\frac{1}{2}} = \frac{1}{2}[\boldsymbol{F}_i + \boldsymbol{F}_{i+1} - (\boldsymbol{W}_i + \boldsymbol{W}_{i+1})V_\mathrm{t} - |\boldsymbol{A} - V_\mathrm{t}\boldsymbol{I}|^*_{i+\frac{1}{2}}\Delta\boldsymbol{W}] \tag{6}$$

where $|\cdot|^*$ is the Jacobian matrix of ROE's scheme; subscript i, $i+1$ and $i+\frac{1}{2}$ represent left cell, right cell and the interface respectively. $\Delta\boldsymbol{W} = \boldsymbol{W}_{i+1} - \boldsymbol{W}_i$, $\boldsymbol{I}$ is identity matrix.

2.2.5. Precision of numerical scheme

The numerical scheme is of second-order accuracy, which can be derived using the gradient reconstruction technique, and the gradient of flow field variable Φ at cell centers can be calculated by the Green-Gauss law:

$$\nabla\Phi_{\mathrm{c0}} = \frac{1}{V_i}\sum_f \Phi_\mathrm{f} A_\mathrm{f} \tag{7}$$

where Φ_f is the value of Φ at the interface center, V_i the volume of the cell i, A_f the area of the interface and the subscript c0, the center of the control volume. Meanwhile, the limiter of Venkatakrishnan[18] is used here to avoid generating new extrema.

2.2.6. Temporal discretization

A Matrix-Free implicit LU-SGS method[19] for temporal discretization is used, which containsForward sweep:

$$\Delta\boldsymbol{W}^*_i = \boldsymbol{D}^{-1}\left[\boldsymbol{R}_i - \sum\nolimits_{j:j<i}\frac{1}{2}(\Delta\boldsymbol{F}(\boldsymbol{W}^*_j,\boldsymbol{n}_{ij}) - |\lambda_{ij}|\Delta\boldsymbol{W}^*_j)|S_{ij}|\right] \tag{8}$$

Backward sweep:

$$\Delta\boldsymbol{W}_i = \Delta\boldsymbol{W}^*_i - \boldsymbol{D}^{-1}\sum\nolimits_{j:j>i}\frac{1}{2}(\Delta\boldsymbol{F}(\boldsymbol{W}_j,\boldsymbol{n}_{ij}) - |\lambda_{ij}|\Delta\boldsymbol{W}_j)|S_{ij}| \tag{9}$$

where $\boldsymbol{W}_i$ (or $\boldsymbol{W}^*_i$) and $\boldsymbol{W}_j$ (or $\boldsymbol{W}^*_j$)denote the conservative variables of the cell i and j, $\Delta\boldsymbol{W}_i$ (or $\Delta\boldsymbol{W}^*_i$) and $\Delta\boldsymbol{W}_j$ (or $\Delta\boldsymbol{W}^*_j$) denote the increment of conservative variables for cell i and j, $\Delta\boldsymbol{F}$ represents the increment of convective flux, the diagonal matrix is $\boldsymbol{D}_i = \frac{V_i}{\Delta\tau} + \frac{1}{2}\sum_j|\lambda_{ij}||S_{ij}|$, $\boldsymbol{R}_i$ is the residual after the m_{th} iteration in pseudo-time domain, $|\lambda_{ij}|$ is the spectral radius of the flux Jacobian matrix and $|S_{ij}|$ represents the area of the interface. Fig. 7 is the schematic of tilt rotor flow field calculation.

3. Results and discussion

3.1. Induced velocity (dynamic pressure) calculations for an experimental rotor

The experimental rotor model has two untwisted and untapered blades ($R = 0.914$ m) and airfoil section is NACA0012. Operating condition is: blade tip Mach number $M_{\mathrm{tip}} = 0.3285$ and collective angle $\theta_0 = 11°$. Fig. 8 is the comparison between predicted dynamic pressure distributions and experimental data[20] at different axial positions, where r and y represent

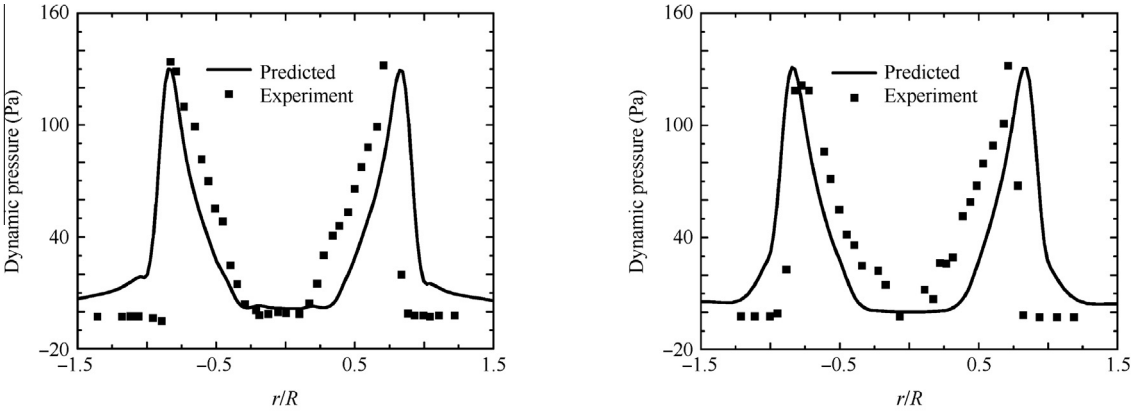

(a) y=–0.215R (b) y=–0.325R

Fig. 8 Comparisons of predicted dynamic pressure distributions with experiment data.

the radial position and axial position. It can be seen from the figure that the calculated results and experimental data agree well.

3.2. Tilt rotor flow fields and aerodynamic characteristics

3.2.1. Tilt rotor grid system

The geometry of tilt rotor used in this paper is shown in Fig. 9, with the rotor modeled as an actuator disk. In order to conveniently describe the relative movement and guarantee grid quality, structured grids are separately generated around fuselage and nacelle which are regarded as background grid and minor grid respectively. The minor grid is totally embedded into background grid, as shown in Fig. 10. The total number of grid cells is approximately 1.5×10^7. As the geometry has a small gap between the wing and nacelle, special care was taken during grid generation to ensure enough overlap region. Meanwhile, grid refinement was made around actuator disk in order to capture dominant flow features and the maximum spacing is less than $0.01c$ (c denotes the airfoil chord length at blade tip). As the solver is based on unstructured embedded grid methods, grids are treated as unstructured during real computation.

3.2.2. Flow fields of tilt rotor in conversion mode

The operating condition in this section is as follows: pitch angle is 20° and free stream velocity is 30 m/s and 50 m/s. Due to the great challenges to the unsteady flow field simulation of tilt rotor aircraft for continuous tilt process, a quasi-steady method is used here and only flow fields at four different tilt angles are calculated. Four spanwise locations are selected for analyzing the chord wise pressure variation. These locations are situated at $0.3R$, $0.5R$, $0.7R$ and $0.85R$ from the rotor center and noted as Position 1, Position 2, Position 3 and Position 4 respectively, as shown in Fig. 11.

As we know, down wash induced by rotor decreases the actual angle of wing sections. Pressure distributions on the above wing locations at different rotor tilt angles are presented in Fig. 12, the symbol z/c on horizontal axis represents the nondimensional airfoil chord length. It can be seen from the figure that the pressure difference among the upper and lower airfoil sections grows up with the tilt angle increasing, which means the wake effect is weakening with the tilt angle increasing. However, there is an exception that no obvious regularity is found at Position 1, as it locates near the conjunction of wing and nacelle, which may lead to more complicated flow phenomenon.

Fig. 13 demonstrates pressure distribution on wing Position 3 at different free stream velocities, V. It can be seen from this figure that both the negative pressure on the upper surface and the positive pressure on the lower surface decrease with the free stream velocity increasing at the same tilt angle but the changes on the upper surface are much more obvious which leads to the increase of lift. However, there is an exception when the tilt angle is 90°, the negative pressure on the upper surface increases with the free stream velocity increasing which contributes to the decrease of lift. In conclusion, the interaction between rotor wake and other components is complicated which relates to many factors and it changes the aerodynamic characteristic of components behind the rotor.

In order to better elucidate the aerodynamic interaction between rotor and wing, the distribution of rotor thrust is analyzed, as shown in Fig. 14. Fig. 14 shows the rotor thrust coefficient distribution, with the solid line showing the result of wing/rotor model and the dashed line demonstrating that of isolated rotor model, the variables γ and C_T on the horizontal axis and vertical axis denote tilt angle and rotor thrust coefficient. It can be seen from the figure that rotor thrust decreases with the tilt angle increasing in both cases and rotor thrust is larger in the former case due to the blockage of wing to rotor wake. There is a difference about 5% when the tilt angle is 0° and the discrepancy appears a declining tendency with the tilt angle increasing.

Fig. 15 demonstrate pressure fields and streamlines distributions on typical wing section, which is situated at $0.7R$ from

Fig. 9 Geometry of tilt rotor.

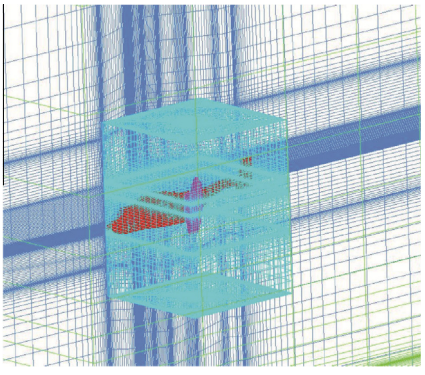

Fig. 10 Tilt rotor grid system.

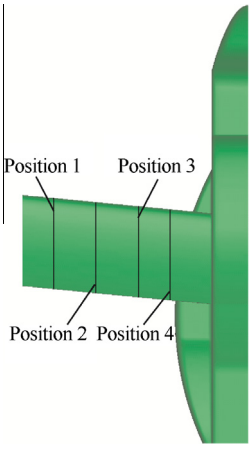

Fig. 11 Spanwise stations on the wing.

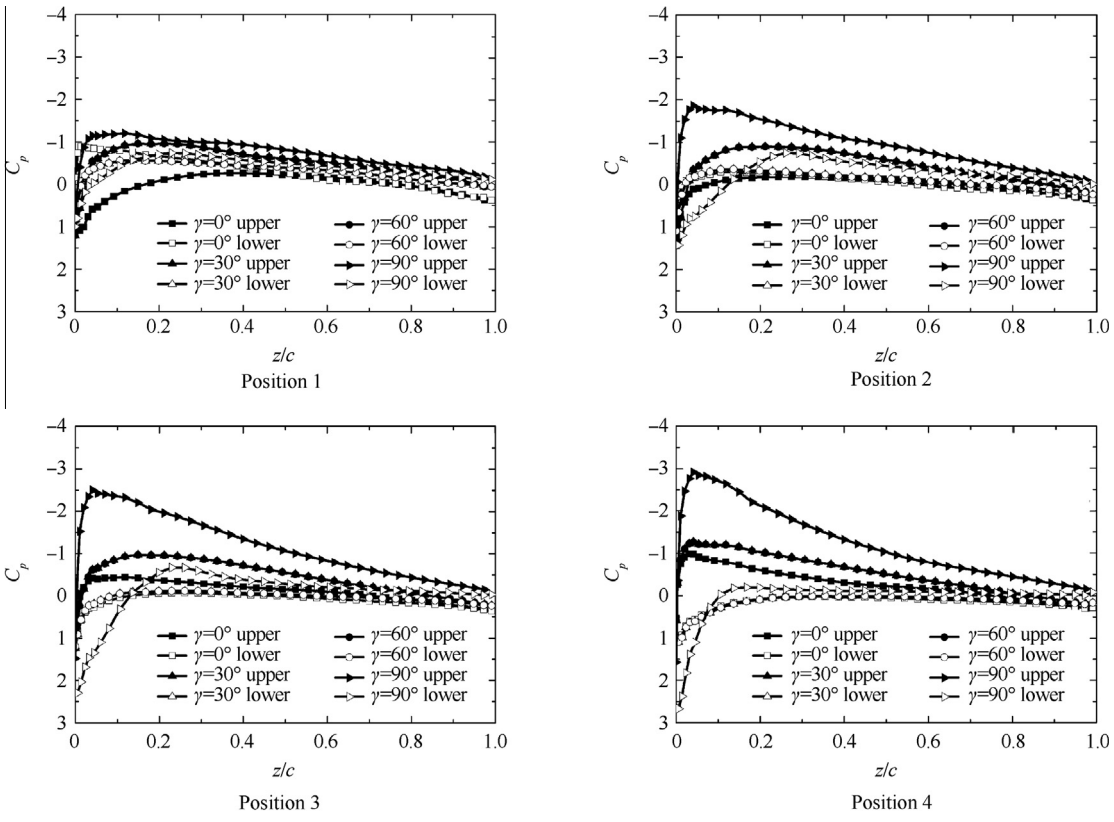

Fig. 12 Pressure distributions on wing locations at different tilt angles.

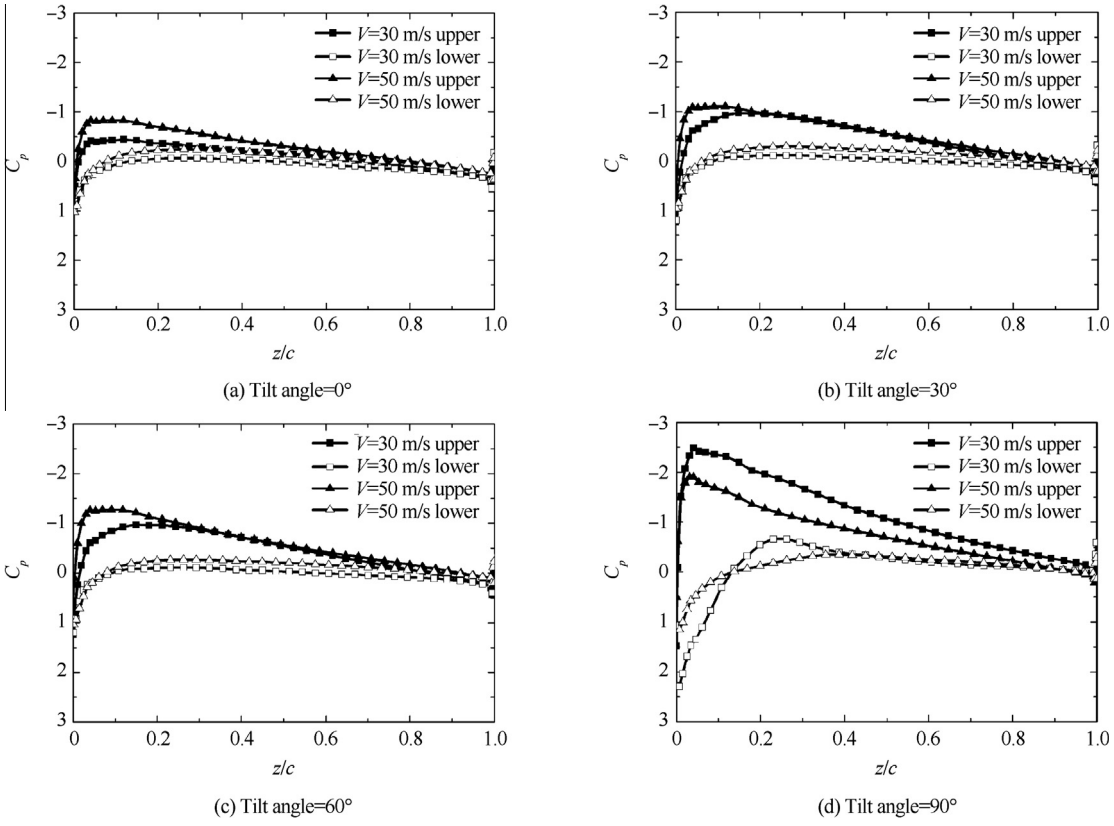

Fig. 13 Pressure distributions on wing position3 at different free stream velocities.

the rotor center, at different rotor tilt angles for the above two free stream velocities respectively. It can be concluded that inflow is deflected and accelerated through the actuator disk and deflection effect is weakening with the tilt angle increasing. In addition, it can also be seen by comparing these two figures that the inflow is less deflected by actuator disk with the increase of free stream velocity at the same tilt angle, which is particularly obvious when tilt angle is 0°.

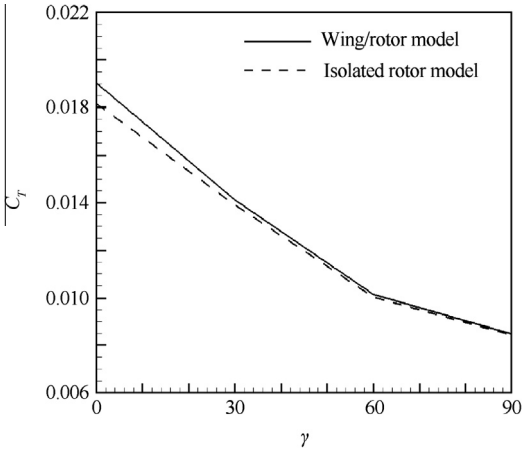

Fig. 14 Rotor thrust coefficient distribution.

Fig. 16 shows pressure contour on fuselage and actuator surface. It can be seen from this figure that the flow induced by rotors impacts the upper wing and produces a large area of high pressure, and the influence range changes with the tilt angle variation.

Fig. 17 illustrates streamline distributions on typical section (perpendicular to z axis and through the rotor rotation center). It can be seen from the figure that the downwash induced by rotor is blocked by wing and partial flow runs inward along the wing span then concentrates near the region of symmetry plane of fuselage and eventually deflects upward, giving birth to the rotor fountain flow, as the forward flight speed is not very high. The fountain flow phenomenon disperses with tilt angle increasing, as the rotor wake direction deflection gets weakened and less blocked by the wing. The flow structure is similar when the free stream velocity is 50 m/s and no more detailed figures are given here.

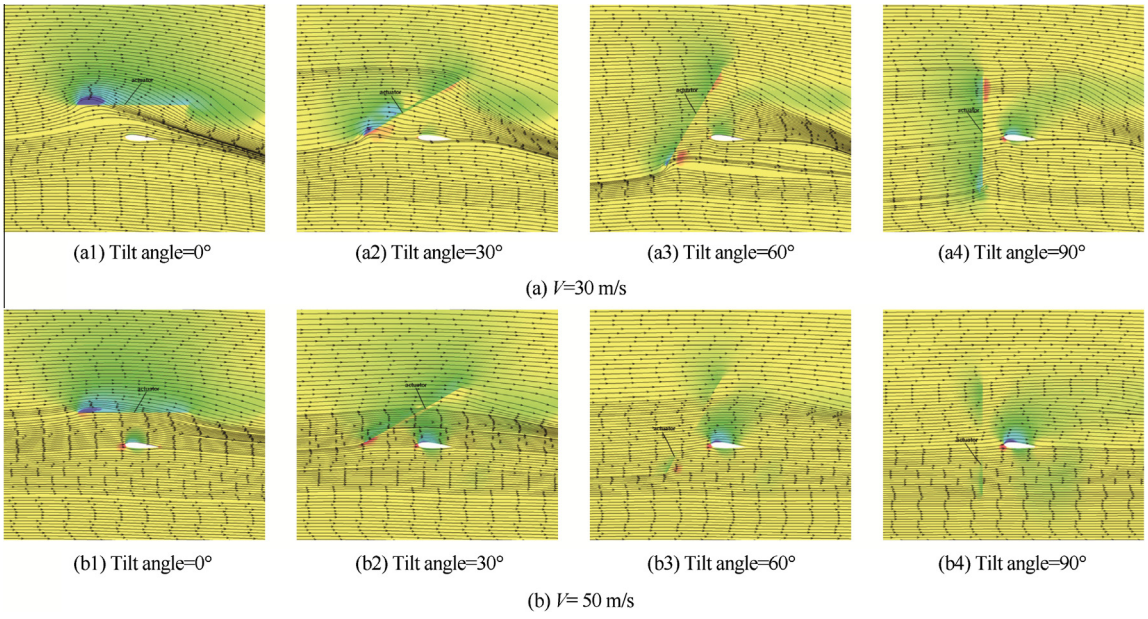

Fig. 15 Pressure fields and distributions of streamlines on typical wing section at different tilt angles.

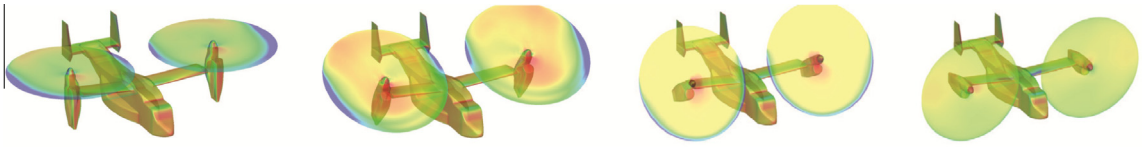

Fig. 16 Pressure contour on fuselage and actuator surface at different tilt angles.

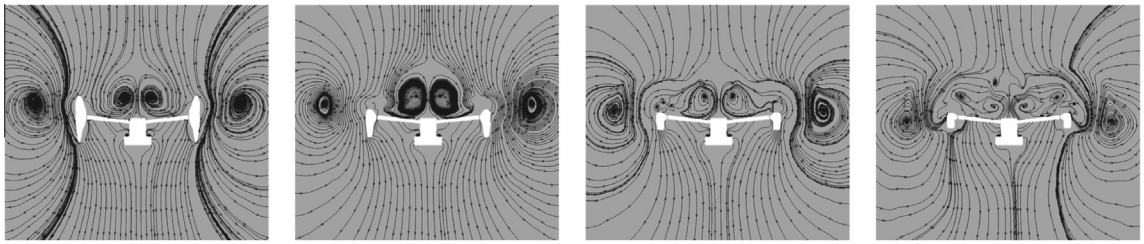

Fig. 17 Streamline distributions on typical section of tilt rotor at different tilt angles(V = 30 m/s).

4. Conclusions

(1) The developed CFD solver is able to capture essential flow characteristics and predict aerodynamic interactions of tilt rotor aircraft in conversion mode.
(2) The transformation relation between different coordinate systems is deduced which successfully extends the utility of actuator disk model to rapid flow field calculation at different tilt angles.
(3) The new method for 'hole cutting' and 'donor searching' proposed is effective for grid assembling and flow fields simulation of tilt rotor in conversion mode.

Acknowledgement

I would like to express my appreciation to my colleague Sun Xiaoling for her help with the modification of English expression in the manuscript.

References

1. Johnson W, Yamauchi GK, Derby MR, Wadcock AJ. Wind tunnel measurements and calculations of aerodynamic interactions between tiltrotor aircraft. Reston: AIAA; 2003. Report No.: AIAA-2003-47.
2. Matuska D, Dale A, Lorber P. Wind tunnel test of a variable-diameter tiltrotor (VDTR) model. Washington, D.C: NASA; 1994 Jan. Report No.: NASA CR177629.
3. Darabi A, Stalker A, McVeigh M, Wygnanski I. The rotor wake above a tiltrotor airplane-model in hover. Reston: AIAA; 2003 Jun. Report No.: AIAA-2003-35963.
4. Meakin RL. Unsteady simulation of the viscous flow about a V-22 rotor and wing in hover. Reston: AIAA; 1995. Report No.: AIAA-95-3463-CP.
5. Tai TC. Simulation and analysis of V-22 tiltrotor aircraft forward flight flowfield. *J Aircraft* 1996;**33**(2):369–76.
6. Gupta V, Baeder JD. Investigation of quad tiltrotor aerodynamics in forward flight using CFD. Reston: AIAA; 2002. Report No.: AIAA-2002-2812.
7. Lee-Rausch EM, Biedron RT. Simulation of an isolated tiltrotor in hover with an unstructured overset-grid RANS solver. *American helicopter society 65th annual forum*; 2009 May 27–29; Grapevine, TX. 2009.p. 1–19.
8. Potsdam MA, Strawn RC. CFD simulation of tiltrotor configurations in hover. *American helicopter society 58th annual forum*; 2002 Jun 11–13; Montreal, Canada, 2002.
9. Gupta V. *Quad tilt rotor simulations in helicopter mode using computational fluid dynamics*. Maryland: University of Maryland; 2005 [dissertation].
10. Liu JX. *Unsteady CFD simulations of moving flow-control valves by an unstructured overset grid method*. West Lafayette: Purdue University; 2008 [dissertation].
11. Lee Y, Baeder JD. Implicit hole cutting – A new approach to overset grid connectivity. Reston: AIAA; 2003. Report No.: AIAA-2003-4128.
12. Wang B, Zhao QJ, Xu G. A new moving-embedded grid method for numerical simulation of unsteady flow-field of helicopter rotor in forward flight. *Acta Aerodyn Sin* 2013;**30**(1):14–21 [Chinese].
13. Sitaraman J, Floros M, Wissink A, Potsdam M. Parallel domain connectivity algorithm for unsteady flow computations using overlapping and adaptive grids. *J Comput Phys* 2010;**229**(12):4703–23.
14. Madrane A, Heinrich R, Gerhold T. Implementation of the embedded method in unstructured hybrid DLR finite volume Tau-code. *6th overset composite grid and solution technology symposium*; 2002 Oct.; Walton Beach, Florida, USA. 2002.
15. Bonet J, Peraire J. An alternate digital tree (ADT) algorithm for 3D geometric searching and intersection problems. *Int J Numer Methods Eng* 1991;**31**:1–17.
16. Rajagopalan RG, Mathur SR. Three dimensional analysis of a rotor in forward flight. *Proceedings of AIAA 20th fluid dynamics, plasma dynamics and lasers conference*; 1989 Jun 12–14; New York, USA. 1989. p. 1–12.
17. Roe PL. Approximate Riemann solvers, parameter vectors, and difference schemes. *J Comput Phys* 1981;**43**(2):357–72.
18. Venkatakrishnan V. On the accuracy of limiters and convergence to steady state solutions. Reston: AIAA; 1993. Report No.: AIAA-1993-0880.
19. Luo H, Baum JD. A fast, matrix-free implicit method for computing low Mach number flows on unstructured grids. Reston: AIAA; 1999. Report No.: AIAA-1999-3315.
20. McKee JW, Naeseth RL. Experimental investigation of the drag of flat plates and cylinders in the slipstream of a hovering rotor. Washington, D.C.: Langley Aeronautical Laboratory; 1958 Apr. Report No.: NACA-TN-4239.

Zhang Ying received the master's degree in computational fluid dynamic from Beihang University in 2011, and then became an employee in AVIC Aerodynamics Research Institute. Her main research interest is CFD.

Ye Liang is a senior engineer in AVIC Aerodynamics Research Institute. He received his doctor's degree in aircraft design from Nanjing University of astronauts and astronautics in 2009. His area of research is mainly CFD on rotor aircraft.

Yang Shuo is an engineer in AVIC Aerodynamics research institute. She received the master's degree in aircraft design from Beihang University in 2012. Her current research interest is CFD.